

Self-assembly of polyhedral metal-organic framework particles into three-dimensional ordered superstructures

Civan Avci¹, Inhar Imaz¹, Arnau Carné-Sánchez¹, Jose Angel Pariente², Nikos Tasios³, Javier Pérez-Carvajal¹, Maria Isabel Alonso⁴, Alvaro Blanco², Marjolein Dijkstra³, Cefe López^{2*} and Daniel Maspoch^{1,5*}

Self-assembly of particles into long-range, three-dimensional, ordered superstructures is crucial for the design of a variety of materials, including plasmonic sensing materials, energy or gas storage systems, catalysts and photonic crystals. Here, we have combined experimental and simulation data to show that truncated rhombic dodecahedral particles of the metal-organic framework (MOF) ZIF-8 can self-assemble into millimetre-sized superstructures with an underlying three-dimensional rhombohedral lattice that behave as photonic crystals. Those superstructures feature a photonic bandgap that can be tuned by controlling the size of the ZIF-8 particles and is also responsive to the adsorption of guest substances in the micropores of the ZIF-8 particles. In addition, superstructures with different lattices can also be assembled by tuning the truncation of ZIF-8 particles, or by using octahedral UiO-66 MOF particles instead. These well-ordered, sub-micrometre-sized superstructures might ultimately facilitate the design of three-dimensional photonic materials for applications in sensing.

Spherical colloidal particles (mainly silica or polymers such as polystyrene and acrylates) have traditionally been used to build self-assembled superstructures^{1–4}. They tend to pack into the entropically favoured face-centred cubic (fcc) arrangement, although they can also adopt the less favoured, hexagonal close-packed (hcp) structure or the random, hexagonally close-packed (rhcp) lattice. Recently, the self-assembly of non-spherical polyhedral particles has begun to be considered as a viable method to diversify possible packing geometries^{5–10}, including the formation of crystals, liquid crystals, plastic crystals and quasicrystals^{8,11,12}. Presently, these particles (mainly, metallic and metal chalcogenide particles such as gold^{13,14}, silver^{15,16}, cadmium/lead selenide/sulfide^{17–19} and manganese oxide)²⁰ can be synthesized in multiple shapes, with high monodispersity and good colloidal stability, and can be coated with multiple organic polymers. Accordingly, several groups have observed, both experimentally and through simulations, that polyhedral particles form long-range ordered assemblies, corresponding to their densest packing, by alignment of the particle facets to maximize the entropy of the system^{9,12,14,15,21,22}.

So far, only a few studies have illustrated the use of polyhedral particles to generate long-range ordered arrangements that pack into different lattices. For example, Yang and co-workers have shown that polyvinylpyrrolidone-coated cubic, octahedral and truncated octahedral silver particles (dimensions of 100–300 nm) can be self-assembled by gravitational sedimentation into their corresponding densest lattice packings: the cubic, space-filling Kelvin structure or Minkowski packings, respectively¹⁵. Wang and co-workers demonstrated that, depending on their shape,

cetyltrimethylammonium bromide (CTAB)-coated gold nanoparticles can self-assemble by water evaporation into different lattices¹³. They described self-assembly of gold rods, polyhedra, cubes and bipyramids into nematic/smectic-A, hexagonally packed, tetragonally packed and nematic/three-dimensionally ordered arrangements. More recently, Mirkin and co-workers have shown that depletion-based assembly allows cetyltrimethylammonium chloride (CTAC) or CTAB-coated gold nanoparticles with different shapes (rhombic dodecahedra, truncated cubes and octahedra) to self-assemble into multiple lattices (fcc, simple cubic and body-centred cubic, respectively) that are stable both in solution and in the solid state¹⁴.

Strangely, rapid progress in the self-assembly of inorganic-based polyhedral particles has not led to the use of other families of the purely organic or hybrid metal-organic materials that are usually found as crystalline polyhedral particles, as functional building blocks to construct long-range self-assembled superstructures. The use of such crystalline particles has been precluded mainly by limited control over monodispersity, particle-shape homogeneity and colloidal stability. Here, we report that colloidal crystalline polyhedral MOF particles (in this case, zeolitic imidazolate framework-8 (ZIF-8)^{23,24} and Universitetet i Oslo-66 (UiO-66)²⁵) can be synthesized with the required size and shape homogeneity to subsequently self-assemble into well-ordered three-dimensional superstructures. These MOF-based superstructures show interesting features arising from their structures, in particular a photonic bandgap. Self-assembled spherical colloidal particles (mainly silica, polystyrene and acrylates) can form photonic crystals because they tend to order into superstructures capable of reflecting

¹Catalan Institute of Nanoscience and Nanotechnology (ICN2), CSIC and The Barcelona Institute of Science and Technology, Campus UAB, Bellaterra, 08193 Barcelona, Spain. ²Materials Science Factory, Instituto de Ciencia de Materiales de Madrid (ICMM), Consejo Superior de Investigaciones Científicas (CSIC), Calle Sor Juana Inés de la Cruz, 3, 28049 Madrid, Spain. ³Soft Condensed Matter, Debye Institute for Nanomaterials Science, Utrecht University, Princetonplein 5, 3584 CC Utrecht, the Netherlands. ⁴Institut de Ciència de Materials de Barcelona (ICMAB-CSIC), Campus UAB, 08193 Bellaterra, Spain. ⁵ICREA, Pg. Lluís Companys 23, 08010 Barcelona, Spain. *e-mail: c.lopez@csic.es; daniel.maspoch@icn2.cat

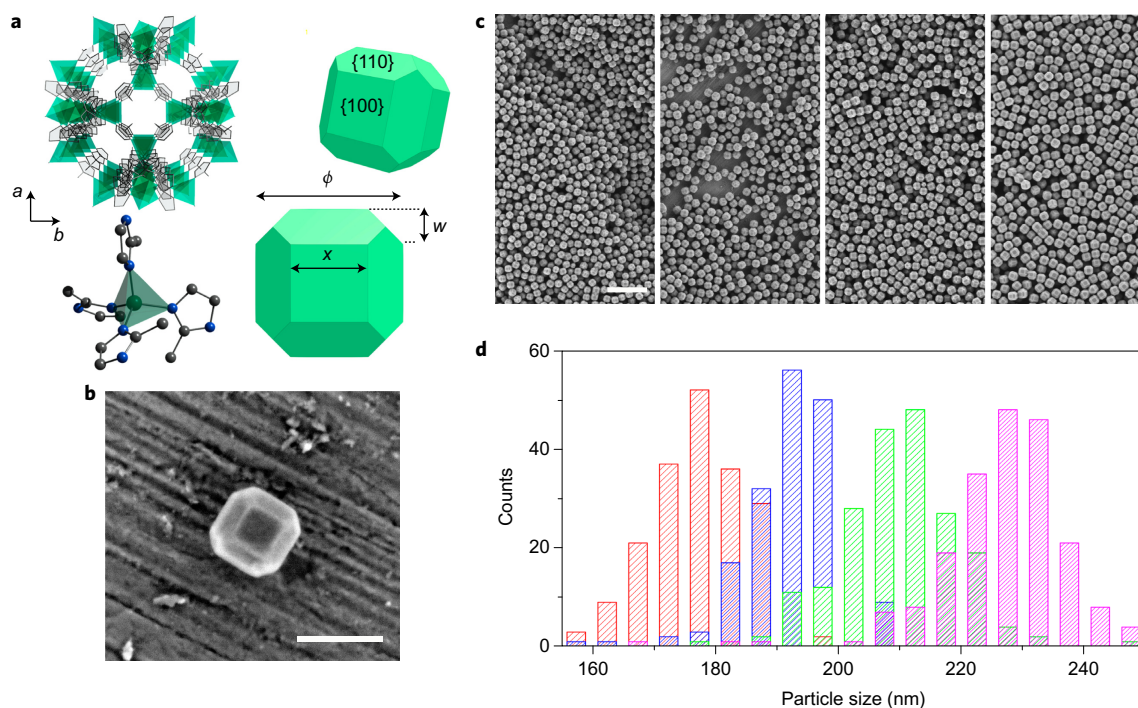


Figure 1 | Structure and characterization of the TRD ZIF-8 particles. **a**, Representation of the crystal structure of ZIF-8 showing that it is formed by the connection of tetrahedral Zn(II) ions (in green) through 2-methylimidazolate (2-MiM) linkers (in grey, top left). Bottom left: environment around one zinc centre. Atom colour code: Zn, green; C, grey; N, blue. Right: schematic illustrations of the ZIF-8 TRD particles, showing the {110} and {100} facets (top) and highlighting: particle size ϕ ; edge length x of the {100} square facets; and chamfer w (bottom). **b**, Representative FE-SEM image of a single TRD ZIF-8 particle. **c**, Representative FE-SEM images of TRD ZIF-8 particles of different sizes. From left to right: 178 ± 8 nm, 193 ± 8 nm, 210 ± 10 nm and 227 ± 10 nm. **d**, Size-distribution histograms of TRD ZIF-8 particles of different sizes: red, 178 ± 8 nm; blue, 193 ± 8 nm; green, 210 ± 10 nm; and purple, 227 ± 10 nm. Scale bars: 200 nm (**b**) and $1 \mu\text{m}$ (**c**).

Table 1 | Length parameters of the particles. Lattice parameters and angles, interplanar distances, optical bandgaps and reflectance of the self-assembled superstructures.

Particle size ϕ (nm)*	x (nm)*	w (nm) [†]	t [‡]	Lattice parameters a, b, c (nm) [§]	Lattice angles γ, β, α (deg)	Interplanar distance d (nm) [¶]	Bandgap (nm) [#]	Reflectance (%) [#]
178 ± 8	93 ± 4	43 ± 2	0.68	188	61	156	461	47
193 ± 8	101 ± 4	46 ± 2	0.69	204	61	169	500	50
210 ± 10	110 ± 5	50 ± 2	0.69	222	61	184	552	57
227 ± 10	119 ± 5	54 ± 2	0.69	239	61	199	600	43

*Measured from FE-SEM images. [†]Calculated from $(\phi - x)/2$. [‡]Calculated from $x/(x + w)$. [§]Calculated from $(2w^2 + \phi^2)^{1/2}$. ^{||}Calculated from $\cos^{-1}[(w^2 + 2\phi w)/(2w^2 + \phi^2)]$. [¶]Calculated from $[2w(w^2 - \phi w) + \phi(\phi^2 - w^2)]/[2(w^2 - \phi w)^2 + (\phi^2 - w^2)^2]^{1/2}$. [#]Measured from UV-vis reflectance spectra.

light at specific wavelengths and directions (photonic bandgap) due to the periodic refractive index distribution they create^{2,3}. Here, the photonic bandgap of the MOF-based superstructures can not only be tuned by controlling the size of the MOF particles, but is also responsive to the sorption of guest substances.

Results and discussion

Synthesis of truncated rhombic dodecahedral ZIF-8 particles.

Highly monodisperse sub-micrometre-sized colloidal truncated rhombic dodecahedral (TRD) ZIF-8 particles in water were fabricated and stabilized by using CTAB as a cationic surfactant and a capping agent (Fig. 1a,b). ZIF-8 is a porous MOF made of Zn(II) ions and 2-methylimidazolate (2-MiM) linkers that exhibits a sodalite-type structure, a large surface area ($\sim 1,200$ – $1,500 \text{ m}^2 \text{ g}^{-1}$), good chemical and thermal stability, and is suited to many interesting porosity-related applications (for example, gas storage, separation and catalysis)^{23,24,26}. ZIF-8 first crystallizes into cubic-shaped seeds, which gradually evolve into TRD particles and, finally, into the thermodynamically more stable rhombic

dodecahedral (RD) particles due to the predominant (100) growth^{27,28}. In this process, CTAB facilitates the synthesis of TRD ZIF-8 particles, as it selectively attaches to the {100} facets (*vide supra*)²³. By controlling the amount of CTAB and 2-MiM, well-defined TRD ZIF-8 particles with sizes ranging from 178 ± 8 nm to 227 ± 10 nm were synthesized (with ϕ defined as the distance between opposing square facets; Fig. 1c,d and Table 1). In all cases, their size dispersity was $\sim 5\%$. The TRD ZIF-8 particles exhibit six {100} square facets with edge length x (Fig. 1a and Table 1) and twelve {110} irregular hexagonal facets with a surface area ratio of $\sim 1:1.5$ ({100}:{110}). These TRD particles, which can also be viewed as chamfered cubes (that is, cubes with bevelled edges), have a chamfer w that increases with ϕ and a constant truncation t of 0.68–0.69 (Table 1). X-ray powder diffraction (XRPD) indicated that all particles are crystalline ZIF-8 (Supplementary Fig. 1). Nitrogen physical sorption measurements on the ZIF-8 particles validated their microporosity. The measured Brunauer–Emmett–Teller (BET) surface area ($1,154 \text{ m}^2 \text{ g}^{-1}$) is fully consistent with previously reported values for ZIF-8²³

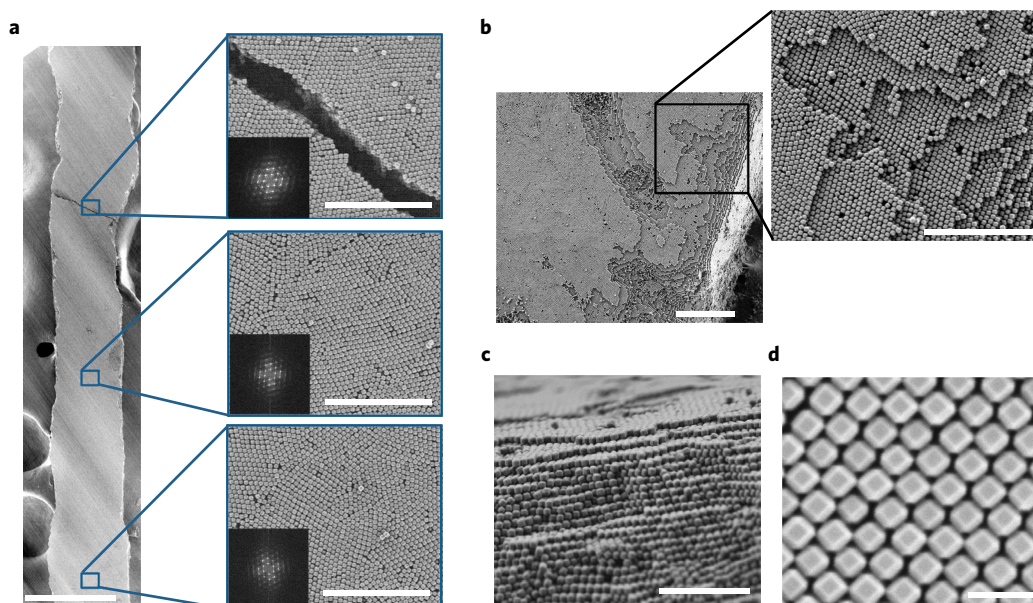


Figure 2 | Ordered rhombohedral self-assembled superstructures. Representative FE-SEM images of a self-assembled superstructure made of TRD ZIF-8 crystals (size 210 ± 10 nm). **a**, Low-magnification image of a self-assembled superstructure that extends over 1 mm. The three magnified sections reveal that the rhombohedral lattice is maintained across the self-assembled superstructure. Note here that—as in any other superstructure made of self-assembled particles—the ordering of TRD ZIF-8 crystals reveals domains with misfit dislocations and point defects. Insets: Fourier transforms of these sections showing different grain orientations. **b**, Edge of a self-assembled superstructure, showing order in the three dimensions. **c**, Cross-section of the self-assembled superstructure. **d**, Zoom of the packing structure. Scale bars: 200 μm (**a**), 5 μm (**a**, insets), 10 μm (**b**), 1 μm (**b**, inset), 2 μm (**c**) and 500 nm (**d**).

(Supplementary Fig. 2) and can be accounted for by internal porosity, as the external surface of the ZIF-8 is negligible in comparison.

Self-assembly of TRD ZIF-8 particles. In the self-assembly experiments, TRD ZIF-8 particles arranged into millimetre-sized three-dimensional superstructures by evaporation under heating. We began by placing a droplet of an aqueous colloidal solution of the particles (100 mg ml^{-1}) on a clean glass surface. Then, the surface was incubated in an oven at 65°C until the droplet was dried. Field-emission scanning electron microscopy (FE-SEM) of the resulting dried solids revealed the formation of self-assembled superstructures in which the ZIF-8 particles are ordered along the three directions of space (Fig. 2 and Supplementary Fig. 3). The initial evaporation temperature optimized to ensure homogeneous three-dimensional ordering along the entire monolithic structure was found to be $\sim 65^\circ\text{C}$. Evaporation at room temperature yielded three-dimensional ordering but led to heterogeneity in the monolith thickness by generating thick surrounding walls around the droplet, which were formed by a concave meniscus formed over time (Supplementary Fig. 4). In contrast, a higher temperature (100°C) led to quasi-amorphous packings caused by faster evaporation (Supplementary Fig. 4). Interestingly, other tested techniques, such as dip- and spin-coating, vertical deposition and even simple centrifugation, all yielded similar self-assembled superstructures. However, in these cases the observed degree of three-dimensional ordering was much lower (Supplementary Figs 4 and 5).

Upon self-assembly, the TRD ZIF-8 particles adopted the densest rhombohedral packing, with a packing fraction of 0.86 (Figs 2 and 3a). Investigations using Floppy-Box Monte Carlo simulations based on a simulating-annealing approach in which the densest crystal structure is predicted by slowly increasing the pressure, also resulted in the formation of the same rhombohedral packing (Fig. 3b)^{30,31}. The packing that we observed resulted from maximizing the density of the TRD particles. As

shown in Fig. 3c–f, the maximum number of neighbours that can be adjacent to a given TRD particle is twelve (Fig. 3f). Of these neighbours, six are perfectly aligned through hexagonal $\{110\}$ facets (in two groups of three that meet at two diagonally opposing vertices; Fig. 3c), whereas the remaining six are connected through square $\{100\}$ facets (Fig. 3d). In these latter connections, the $\{100\}$ facets of neighbouring particles are touching and aligned but with a small shift (equal to w) in the two directions defined by the sides of the square (Fig. 3e). The resulting structure exhibits a rhombohedral Bravais lattice with a unit cell with lattice parameters \vec{a} , \vec{b} and \vec{c} and angles γ , β and α , as described in Table 1.

Photonic crystal properties. The MOF-based superstructures introduced here are periodic dielectrics made of ~ 200 nm MOF particles that also show angle-dependent opalescence arising from a photonic bandgap. Moreover, because the lattice period is comparable to visible wavelengths, this opalescence is visible to the naked eye (Fig. 4a). Figure 4b presents spectra recorded for superstructures assembled from TRD ZIF-8 particles of different sizes. These spectra were measured using reflectance spectrophotometry at normal incidence ($\theta = 0^\circ$). A clear band in the optical reflectance spectrum was observed that is attributed to the opening of a bandgap in the (001) direction in reciprocal space, which is associated with the Bragg reflection from the (001) crystallographic planes of the rhombohedral lattice. Notice that these layers are not parallel to the square facet of the particles but form an angle given by $\cos \delta = (001) \cdot \vec{a} \times \vec{b} / |\vec{a}| |\vec{b}| = (\phi^2 - w^2) / (\phi^2 + 2w^2)$. The magnitude of reflectance ranged from 40 to 57% (Table 1 and Supplementary Fig. 6), which is comparable with standard literature values for self-assembled three-dimensional photonic crystals made of spherical particles³. The reflectance spectra also showed (1) the Bragg reflection spectral position scales with particle size and (2) as expected, the Bragg reflection shifted linearly towards shorter wavelengths at smaller particle sizes.

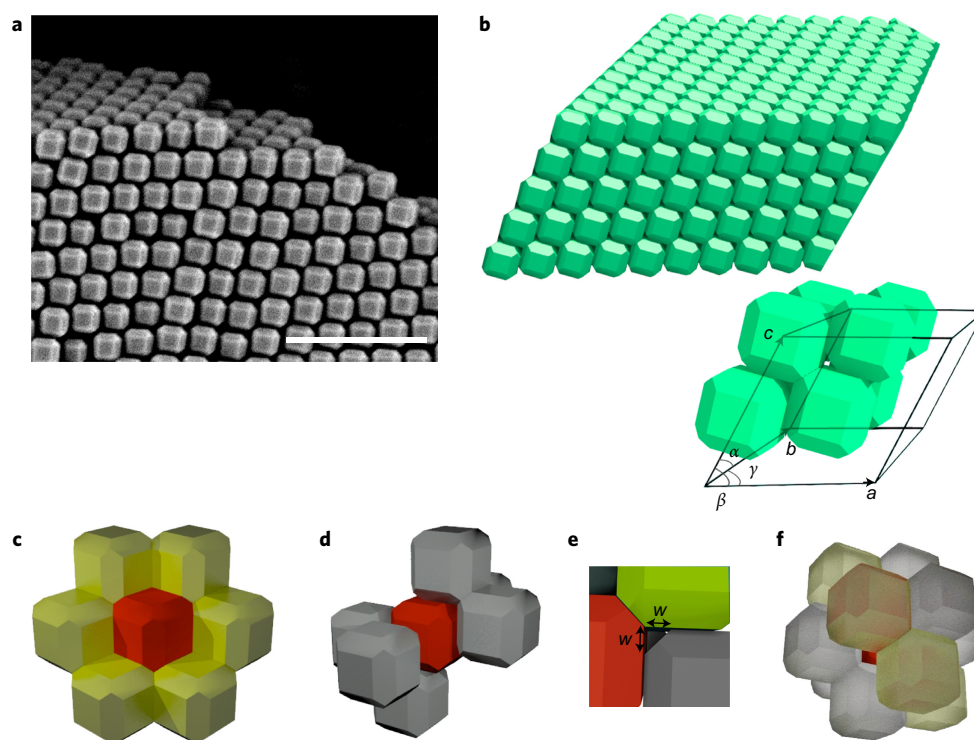


Figure 3 | Computer simulation and FE-SEM image of the formation of the densest rhombohedral lattice. **a**, Representative FE-SEM image of a cross-section of the self-assembled superstructure, showing the rhombohedral lattice. **b**, Densest packing obtained from Floppy-Box Monte Carlo simulations, confirming the same type of rhombohedral lattice obtained experimentally. Bottom right: unit cell of the rhombohedral lattice. **c–f**, Schematics showing the connectivity of a single TRD ZIF-8 particle in the rhombohedral lattice: six TRD particles perfectly aligned through the {110} facets (**c**); six TRD particles aligned through the {100} facets (**d**); representation showing the shift in two directions of these latter connections (**e**); combined 12 TRD particles aligned to a single TRD particle (**f**). Scale bar in **a**: 1 μm .

Figure 4c shows the Bragg reflection maximum or bandgap centre (λ_c) plotted against the interplanar distance d . Here, it is possible to fit λ_c using the Bragg–Snell law for normal incidence, which is defined as $\lambda_c = 2nd$, where n is the effective index of refraction of the superstructure. For our rhombohedral superstructure we calculated the interplanar distances by taking the normalized cross product of lattice vectors \vec{a} and \vec{b} , which gives the normal to the plane defined by \vec{a} and \vec{b} (Table 1). Thus, from the slope of the fitted curve, we determined an effective refractive index of 1.49. This value is very close to the value (1.47) calculated by averaging the dielectric constant $\varepsilon = V_{\text{fram}}(n_{\text{fram}})^2 + V_{\text{H}_2\text{O}}(n_{\text{H}_2\text{O}})^2 + V_{\text{air}}(n_{\text{air}})^2$, where V and n are the volume fractions and effective refractive indexes of the different components, respectively (Supplementary Section 2 and Supplementary Table 1). This value of 1.49 is also in good agreement with the value (1.43) obtained by spectroscopic ellipsometry performed on the photonic crystal self-assembled from 210 nm TRD ZIF-8 particles (Supplementary Fig. 7)³². Importantly, the closely linear relationship between the interplanar distance (or particle size) and the maximum reflection wavelength (Fig. 4c) is a clear indication that the product packing fraction times average refractive index remains constant throughout the explored particle size range. That the refractive index of the MOF does not vary should not be surprising, given that all the TRD ZIF-8 particles are synthesized under the same conditions. However, only particles for which the proportions are preserved assemble into structures with the same packing fraction, as this is determined by the w/x ratio. As observed in Table 1, w very closely follows a linear relationship with x (Supplementary Fig. 8). This indicates that the self-assembly proceeds similarly in all cases and is consistent with the fact that all the particles in the studied size range have the same geometry.

The microporosity of MOFs highly favours the use of these photonic structures for the development of sensing applications, because the adsorption of species in the MOF pore network can change their refractive index, resulting in a pronounced shift in the photonic bandgap spectral position λ_c . To realize this, the porous MOF particles should be activated, by driving out the water of the ZIF-8 particles without disrupting the well-ordered assembly so as to allow the adsorption of analyte molecules inside the empty pores. To this end, we studied the evacuation of the guest water molecules of the photonic structure self-assembled from 210 nm TRD ZIF-8 particles by heating it at 260 °C, a temperature at which thermogravimetric analysis (TGA) assured the complete removal of water molecules (Supplementary Fig. 9). Indeed, TGA of the heated superstructure indicated that no further weight loss had occurred up to 300 °C (Supplementary Fig. 9), confirming that all guest water molecules had been evacuated. Moreover, FE-SEM images demonstrated preservation of the rhombohedral packing, whereas an N_2 isotherm illustrated the typical type-I behaviour consistent with a BET surface area of 1,250 $\text{m}^2 \text{g}^{-1}$, thus confirming the microporous character of the photonic structure (Supplementary Figs 10 and 11). Naturally, in this activated (fully dehydrated) photonic crystal, λ_c displaced to shorter wavelengths (from 552 to 522 nm), which we expect for the replacement of water molecules with air (Supplementary Fig. 12).

As proof of concept, we subsequently exposed the activated photonic crystal to the vapour of different alcohols (methanol, ethanol, isopropanol and *n*-butanol) and to water vapour, while measuring the shift in the photonic bandgap. We found a redshift in λ_c when the photonic crystal was exposed to alcohol vapour (methanol, $\lambda_c = 561 \text{ nm}$; ethanol, $\lambda_c = 562 \text{ nm}$; isopropanol,

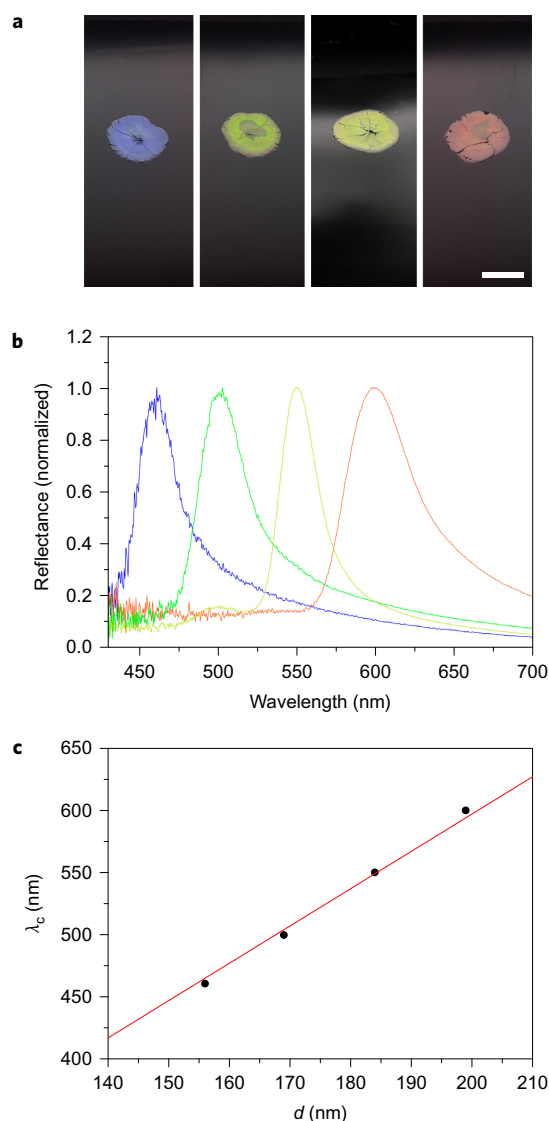


Figure 4 | Photonic properties. **a,b**, Photographs (**a**) and normalized optical reflection at $\theta = 0^\circ$ of the self-assembled photonic crystals made of TRD ZIF-8 particles of different sizes (**b**): 178 ± 8 nm (blue); 193 ± 8 nm (green); 210 ± 10 nm (yellow); and 227 ± 10 nm (red). **c**, Bragg reflection maximum wavelength λ_c plotted against interplanar distance d and fit to the Bragg law (red line) constrained to intercept at zero. Scale bar in **a**: 1 cm.

$\lambda_c = 564$ nm; *n*-butanol, $\lambda_c = 568$ nm; Supplementary Figs 13 and 14) but not when it was exposed to water. This selectivity is somewhat expected for the inherent selective adsorption properties of ZIF-8, which is known to absorb alcohols but not water³³. Considering a pore filling of 81% for methanol, ethanol or isopropanol and 86% for *n*-butanol (calculated from the adsorption isotherms; Supplementary Fig. 15), we concluded that these shifts correlate well with those calculated according to the corresponding effective refractive indices (determined by averaging the dielectric constant; Supplementary Section 2 and Supplementary Table 1). Thus, the replacement of water molecules with air in the pores of ZIF-8 at relatively low pressures changes the refractive index of the photonic crystal, causing the bandgap to shift. We envision that this feature could be exploited for the use of these materials as responsive materials or sensors.

Extending the self-assembly to MOF particles with other morphologies. Having demonstrated that well-ordered arrays can

be fabricated from TRD ZIF-8 particles, we considered that the numerous MOFs reported to date could be an excellent source of crystalline polyhedral particles. We inferred that control of particle size, shape and self-assembly could enable new packing geometries. To this end, we extended the concept of using MOF particles to spontaneously generate ordered arrays by using ZIF-8 particles with other morphologies (that is, TRD with a lower degree of truncation and non-truncated RD), as well as octahedral particles of the UiO-66 MOF (Fig. 5). For the synthesis of TRD ZIF-8 particles with less truncation ($\phi = 263 \pm 13$ nm; $x = 107 \pm 5$ nm; $w = 78 \pm 4$ nm; $t = 0.57$ versus 0.69 for the previously synthesized TRD ZIF-8 particles), the capping effect of CTAB was reduced to accelerate the growth of the {100} facets (Supplementary Fig. 17). Complete removal of the CTAB resulted in either slightly truncated ($\phi = 319 \pm 14$ nm; $x = 76 \pm 3$ nm; $w = 122 \pm 5$ nm; $t = 0.38$; Supplementary Fig. 17) or non-truncated ($t = 0$) RD ZIF-8 particles, depending on the reaction time. The latter particles exhibited a ϕ (defined as the distance between opposing vertices) of 530 ± 30 nm and an edge size of 230 ± 12 nm (Supplementary Fig. 17).

Experimental observations confirmed that the new ZIF-8 particles self-assemble into ordered arrangements once their colloidal solutions are evaporated off at either 65 °C (TRD particles) or 120 °C (RD particles). A theoretical analysis of the densest packings as a function of t of the ZIF-8 particles is shown in Fig. 5a. We found that the densest packing is a rhombohedral crystal for TRD particles with truncation t higher than 0.66, whereas it is an fcc crystal for t lower than 0.66. These theoretical findings corroborate the experimentally obtained self-assembled superstructures. As shown above, monodisperse TRD ZIF-8 particles with $t = 0.69$ adopted rhombohedral packing, whereas the newly synthesized particles with $t = 0.57$ crystallized into a plastic fcc crystal with a packing fraction of 0.68 (Fig. 5c). Note that the plastic fcc crystal differs from the regular one in the sense that no preferential facet-to-facet interactions exist between neighbouring ZIF-8 particles. We reasoned that the formation of a plastic—rather than a regular—fcc crystal was due to kinetic effects. Consistent with the simulation data, the slightly truncated ZIF-8 particles ($t = 0.38$) and the RD ZIF-8 particles ($t = 0$) each crystallized into an fcc regular crystal (Fig. 5d). In the latter crystals, each ZIF-8 particle is bound to 12 other particles by their 12 identical {110} facets. Importantly, the self-assembly experiments that we ran with as-synthesized, CTAB-free ZIF-8 particles all failed to produce ordered packings, which can be explained by the strong van der Waals attractions between the particles, which are not balanced by ionic surfactants (like CTAB). This result parallels observations on the assembly of polyhedral inorganic particles, in which adsorbed ionic surfactants/polymers on the particle surfaces are crucial to stabilize the suspension against irreversible colloidal aggregation^{14,15}. We wish to remark here that non-adsorbed ionic surfactants/polymers in solution can be used to assist self-assembly by inducing depletion attractions between the particles.

Finally, we extended our approach to another MOF. We synthesized monodisperse octahedral particles of UiO-66²⁵ ($\phi = 340 \pm 30$ nm, defined as the distance between opposing vertices; edge size = 242 ± 18 nm) using acetic acid as a coordination modulator agent (Supplementary Fig. 17)³⁴. UiO-66 is a promising MOF for catalysis and CO₂ capture due to its large surface area ($1,100\text{--}1,400$ m² g⁻¹) and its high hydrothermal, chemical and thermal stability^{35,36}. After synthesis, we functionalized the UiO-66 particles with CTAB and, using the evaporation method at 85 °C, left them to self-assemble. FE-SEM images revealed the formation of an ordered arrangement showing a hexagonal lattice closely related to the Minkowski lattice (Fig. 5b,e), as has been observed for octahedral silver particles¹⁵.

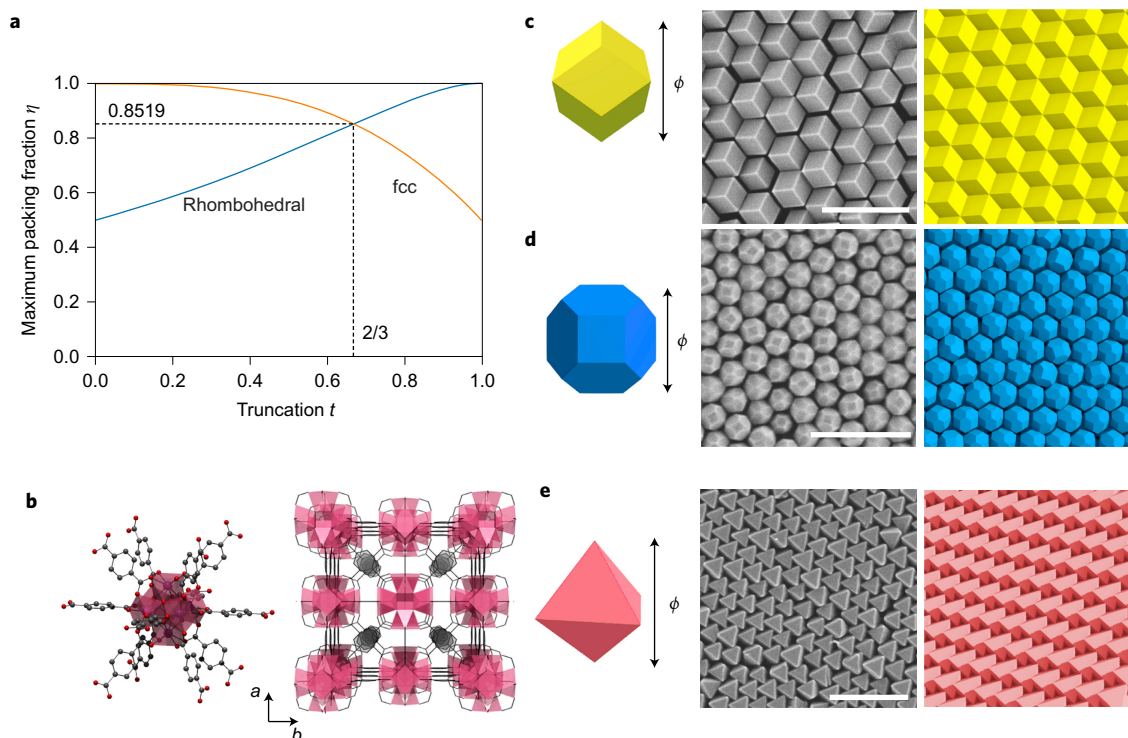


Figure 5 | Ordered self-assembled superstructures made of MOF particles with other morphologies. **a**, Maximum packing fraction η as a function of truncation t of the ZIF-8 particles for the two possible packing geometries: rhombohedral (blue) and fcc (orange). **b**, Representation of the crystal structure of UiO-66, showing that it is formed by connection of hexanuclear $[\text{Zr}_6\text{O}_4(\text{OH})_4]$ oxoclusters through 12 terephthalate linkers (atom colour code: Zr, purple; C, grey; O, red). **c-e**, Left: schematic representation of the single MOF particles of the RD ZIF-8 particles (**c**), TRD ZIF-8 particles with $t = 0.57$ (**d**) and octahedral UiO-66 particles (**e**), respectively. Middle: representative FE-SEM images of the crystals resulting from their respective self-assembly: a plastic fcc crystal (**c**), a regular fcc crystal (**d**) and a hexagonal packing closely related to the Minkowski lattice (**e**). Right: corresponding packings obtained from Floppy-Box Monte Carlo simulations. Scale bars in **c-e**: 1 μm .

Conclusions

We have demonstrated that crystalline, polyhedral TRD ZIF-8 particles can be synthesized with good monodispersity, shape homogeneity and colloidal stability and that they subsequently (spontaneously) self-assemble into millimetre-sized three-dimensional ordered arrangements. The resulting superstructures, corresponding to the densest rhombohedral packings, are porous and show a photonic bandgap functionality that can be tuned by controlling the size of the ZIF-8 particles or by changing the substance adsorbed in the micropores of the ZIF-8 particles. These characteristics should enable the development of self-assembled, MOF-based photonic crystals for sensing applications. In addition, we have extended the formation of ordered arrangements showing different packing geometries to include the self-assembly of crystalline MOF particles with other shapes. These findings show that MOF particles and other molecular crystalline particles, in the same manner as purely organic particles, can be harnessed for the self-assembly of superstructures with long-range periodicities, which is attractive for designing the preparation of materials for applications such as sensing, storage, catalysis and photonics.

Methods

Synthesis of TRD ZIF-8 particles with truncation $t = 0.69$ or 0.57 . In a typical synthesis, $\text{Zn}(\text{CH}_3\text{COO})_2 \cdot 2\text{H}_2\text{O}$ (300 mg) dissolved in 5 ml of water was added to varying amounts of 2-methylimidazole (2-MiM) and CTAB (ref. 29) dissolved in 5 ml of water with gentle stirring for a few seconds. The resulting transparent mixture turned white after 15 s and was left undisturbed at room temperature for 2 h. The resulting ZIF-8 particles were washed three times with deionized (DI) water upon centrifugation at 9,000 r.p.m. in 50 ml Falcon tubes. The collected wet pellets were finally redispersed in DI water at a concentration of 100 mg ml^{-1} . Note that to prevent aggregation, the particles should be dispersed while they are still wet. The zeta potential of the resulting TRD ZIF-8 particles was approximately +40 mV. The

conditions used to synthesize TRD ZIF-8 particles with $t = 0.69$ were the following: for $178 \pm 8 \text{ nm}$, $[\text{CTAB}] = 0.54 \text{ mM}$ and $[2\text{-MiM}] = 2.72 \text{ M}$; for $193 \pm 8 \text{ nm}$, $[\text{CTAB}] = 0.5 \text{ mM}$ and $[2\text{-MiM}] = 2.72 \text{ M}$; for $210 \pm 10 \text{ nm}$, $[\text{CTAB}] = 0.54 \text{ mM}$ and $[2\text{-MiM}] = 2.58 \text{ M}$; for $227 \pm 10 \text{ nm}$, $[\text{CTAB}] = 0.44 \text{ mM}$ and $[2\text{-MiM}] = 2.72 \text{ M}$. The conditions used to synthesize the TRD ZIF-8 particles with $t = 0.57$ were $[\text{CTAB}] = 0.14 \text{ mM}$ and $[2\text{-MiM}] = 3.81 \text{ M}$.

Synthesis of TRD ZIF-8 particles with truncation $t = 0.38$ and RD ZIF-8 particles.

A 5 ml volume of an aqueous solution of $\text{Zn}(\text{CH}_3\text{COO})_2 \cdot 2\text{H}_2\text{O}$ (300 mg) was added to 6.4 ml of an aqueous solution of 2.72 M 2-MiM with gentle stirring. After 15 s the transparent mixture turned white and was then left undisturbed at room temperature for either 15 min (TRD ZIF-8 particles with $t = 0.38$) or 2 h (RD ZIF-8 particles). The resulting ZIF-8 particles were washed three times with DI water with centrifugation at 9,000 r.p.m. in 50 ml Falcon tubes. For functionalization, the particles were redispersed in 0.54 mM CTAB (aq.), stirred for 30 min and washed once more with DI water with centrifugation at 9,000 r.p.m. in 50 ml Falcon tubes. The collected wet pellets were finally redispersed in DI water at a concentration of 100 mg ml^{-1} . The zeta potential of the resulting ZIF-8 particles was approximately +50 mV.

Synthesis of octahedral UiO-66 particles. In a typical synthesis, ZrCl_4 (34.9 mg) and 1-4-benzenedicarboxylic acid (BDC; 24.9 mg) were dissolved in 10 ml of 2.1 M acetic acid (DMF) and transferred to a scintillation vial, which was placed in a pre-heated oven at $120 \text{ }^\circ\text{C}$ for 12 h. The colloidal crystals were then recovered by centrifugation and washed twice with DMF and twice with methanol with centrifugation at 9,000 r.p.m. in a 50 ml Falcon tube. For functionalization, the particles were redispersed in 0.54 mM CTAB (aq.), stirred for 30 min and washed once more with DI water with centrifugation at 9,000 r.p.m. in 50 ml Falcon tubes. The collected wet pellets were finally redispersed in DI water at a concentration of 100 mg ml^{-1} . The zeta potential of the resulting octahedral UiO-66 particles was approximately +50 mV.

Formation of the self-assembled superstructures. Glass microscope slides were initially washed with water and ethanol, dried with a pressurized N_2 gun and subjected to plasma cleaning under Ar^+ for 2 min using a Zepto plasma cleaner (Diener Electronic). Then, 150 μl of each colloidal aqueous solution of MOF particles was added dropwise onto the clean substrate and the treated sample was left

to dry in an oven at varying temperatures. The temperatures used to fabricate the self-assembled superstructures were 65 °C (TRD ZIF-8), 120 °C (RD ZIF-8) or 85 °C (octahedral UiO-66).

Floppy-Box Monte Carlo simulations. To predict the densest crystal structure of hard MOF particles we performed Floppy-Box Monte Carlo simulations^{30,31}. We carried out constant-pressure simulations of $N = 1, 2, 3$ or 4 particles in a simulation box with a variable box shape and periodic boundary conditions. We compressed the system by increasing the pressure stepwise, which enabled us to predict the densest packing. In all cases we obtained the densest packing, as presented in Figs 2 and 3.

Data availability. The data supporting the findings of this study are available upon request from the corresponding author (including data presented in the main text and in the Supplementary Information).

Received 24 July 2017; accepted 13 September 2017;
published online 23 October 2017

References

- Li, F., Josephson, D. P. & Stein, A. Colloidal assembly: the road from particles to colloidal molecules and crystals. *Angew. Chem. Int. Ed.* **50**, 360–388 (2011).
- Von Freymann, G., Kitaev, V., Lotsch, B. V. & Ozin, G. A. Bottom-up assembly of photonic crystals. *Chem. Soc. Rev.* **42**, 2528–2554 (2013).
- Galisteo-López, J. F. *et al.* Self-assembled photonic structures. *Adv. Mater.* **23**, 30–69 (2011).
- Kim, S.-H., Lee, S. Y., Yang, S.-M. & Yi, G.-R. Self-assembled colloidal structures for photonics. *NPG Asia Mater.* **3**, 25–33 (2011).
- Glotzer, S. C. & Solomon, M. J. Anisotropy of building blocks and their assembly into complex structures. *Nat. Mater.* **6**, 557–562 (2007).
- Quan, Z. & Fang, J. Superlattices with non-spherical building blocks. *Nano Today* **5**, 390–411 (2010).
- Damasceno, P. F., Engel, M. & Glotzer, S. C. Predictive self-assembly of polyhedra into complex structures. *Science* **337**, 453–457 (2012).
- Agarwal, U. & Escobedo, F. A. Mesophase behaviour of polyhedral particles. *Nat. Mater.* **10**, 230–235 (2011).
- Torquato, S. & Jiao, Y. Dense packings of the Platonic and Archimedean solids. *Nature* **460**, 876–879 (2009).
- Sacanna, S. & Pine, D. J. Shape-anisotropic colloids: building blocks for complex assemblies. *Curr. Opin. Colloid Interface Sci.* **16**, 96–105 (2011).
- Gantapara, A. P., de Graaf, J., van Roij, R. & Dijkstra, M. Phase diagram and structural diversity of a family of truncated cubes: degenerate close-packed structures and vacancy-rich states. *Phys. Rev. Lett.* **111**, 015501 (2013).
- Haji-Akbari, A. *et al.* Disordered, quasicrystalline and crystalline phases of densely packed tetrahedra. *Nature* **462**, 773–777 (2009).
- Ming, T. *et al.* Ordered gold nanostructure assemblies formed by droplet evaporation. *Angew. Chem. Int. Ed.* **47**, 9685–9690 (2008).
- Young, K. L. *et al.* A directional entropic force approach to assemble anisotropic nanoparticles into superlattices. *Angew. Chem. Int. Ed.* **52**, 13980–13984 (2013).
- Henzie, J., Grünwald, M., Widmer-Cooper, A., Geissler, P. L. & Yang, P. Self-assembly of uniform polyhedral silver nanocrystals into densest packings and exotic superlattices. *Nat. Mater.* **11**, 131–137 (2011).
- Tao, A. R., Ceperley, D. P., Sinsersuksakul, P., Neureuther, A. R. & Yang, P. Self-organized silver nanoparticles for three-dimensional plasmonic crystals. *Nano Lett.* **8**, 4033–4038 (2008).
- Miszta, K. *et al.* Hierarchical self-assembly of suspended branched colloidal nanocrystals into superlattice structures. *Nat. Mater.* **10**, 872–876 (2011).
- Geuchies, J. J. *et al.* *In situ* study of the formation mechanism of two-dimensional superlattices from PbSe nanocrystals. *Nat. Mater.* **15**, 1248–1254 (2016).
- Boneschanscher, M. P. *et al.* Long-range orientation and atomic attachment of nanocrystals in 2D honeycomb superlattices. *Science* **344**, 1377–1380 (2014).
- Xie, S. *et al.* Supercrystals from crystallization of octahedral MnO nanocrystals. *J. Phys. Chem. C* **113**, 19107–19111 (2009).
- Volkov, N., Lyubartsev, A. & Bergström, L. Phase transitions and thermodynamic properties of dense assemblies of truncated nanocubes and cuboctahedra. *Nanoscale* **4**, 4765–4771 (2012).
- Damasceno, P. F., Engel, M. & Glotzer, S. C. Crystalline assemblies and densest packings of a family of truncated tetrahedra and the role of directional entropic forces. *ACS Nano* **6**, 609–614 (2012).
- Park, K. S. *et al.* Exceptional chemical and thermal stability of zeolitic imidazolate frameworks. *Proc. Natl Acad. Sci. USA* **103**, 10186–10191 (2006).
- Huang, X.-C., Lin, Y.-Y., Zhang, J.-P. & Chen, X.-M. Ligand-directed strategy for zeolite-type metal-organic frameworks: zinc(II) imidazolates with unusual zeolitic topologies. *Angew. Chem. Int. Ed.* **45**, 1557–1559 (2006).
- Cavka, J. H. *et al.* A new zirconium inorganic building brick forming metal organic frameworks with exceptional stability. *J. Am. Chem. Soc.* **130**, 13850–13851 (2008).
- Chen, B., Yang, Z., Zhu, Y. & Xia, Y. Zeolitic imidazolate framework materials: recent progress in synthesis and applications. *J. Mater. Chem. A* **2**, 16811–16831 (2014).
- Cravillon, J. *et al.* Controlling zeolitic imidazolate framework nano- and microcrystal formation: insight into crystal growth by time-resolved *in situ* static light scattering. *Chem. Mater.* **23**, 2130–2141 (2011).
- Cravillon, J. *et al.* Formate modulated solvothermal synthesis of ZIF-8 investigated using time-resolved *in situ* X-ray diffraction and scanning electron microscopy. *CrystEngComm* **14**, 492–498 (2012).
- Pan, Y. *et al.* Tuning the crystal morphology and size of zeolitic imidazolate framework-8 in aqueous solution by surfactants. *CrystEngComm* **13**, 6937–6940 (2011).
- de Graaf, J., van Roij, R. & Dijkstra, M. Dense regular packings of irregular nonconvex particles. *Phys. Rev. Lett.* **107**, 155501 (2011).
- Filion, L. *et al.* Efficient method for predicting crystal structures at finite temperature: variable box shape simulations. *Phys. Rev. Lett.* **103**, 188302 (2009).
- Ahles, M. *et al.* Spectroscopic ellipsometry on opaline photonic crystals. *Opt. Commun.* **246**, 1–7 (2005).
- Zhang, K. *et al.* Alcohol and water adsorption in zeolitic imidazolate frameworks. *Chem. Commun.* **49**, 3245–3247 (2013).
- Schaate, A. *et al.* Modulated synthesis of Zr-based metal-organic frameworks: from nano to single crystals. *Chem. Eur. J.* **17**, 6643–6651 (2011).
- Vermoortele, F. *et al.* Synthesis modulation as a tool to increase the catalytic activity of metal-organic frameworks: the unique case of UiO-66(Zr). *J. Am. Chem. Soc.* **135**, 11465–11468 (2013).
- Wu, H. *et al.* Unusual and highly tunable missing-linker defects in zirconium metal-organic framework UiO-66 and their important effects on gas adsorption. *J. Am. Chem. Soc.* **135**, 10525–10532 (2013).

Acknowledgements

This work was supported by EU FP7 ERC-Co 615954, the Spanish MINECO (projects PN MAT2015-65354-C2-1-R and MAT2015-68075-R [SIFE2]) and the Comunidad de Madrid project S2013/MIT-2740 (PHAMA_2.0). It was also funded by the CERCA Programme/Generalitat de Catalunya. The authors based at ICN2 and ICMAB acknowledge the support of the Spanish MINECO through the Severo Ochoa Centers of Excellence Program (grants SEV-2013-0295 and SEV-2015-0496). The authors thank J. Albalad and J. Saiz for their help in the TGA and reflectance measurements, respectively.

Author contributions

C.A. and I.I. synthesized the ZIF-8 particles and the corresponding self-assembled superstructures. A.C.-S. synthesized the UiO-66 particles and the corresponding self-assembled superstructures. N.T. and M.D. performed the Floppy-Box Monte Carlo simulations. C.A., J.A.P., A.B. and C.L. performed and analysed the photonic measurements. M.I.A. performed the ellipsometry characterization, and C.A. and J.P.-C. performed the sorption measurements. D.M. conceived the project and drafted the manuscript. All authors discussed the results and commented on the manuscript.

Additional information

Supplementary information is available in the [online version of the paper](#). Reprints and permissions information is available online at www.nature.com/reprints. Publisher's note: Springer Nature remains neutral with regard to jurisdictional claims in published maps and institutional affiliations. Correspondence and requests for materials should be addressed to C.L. and D.M.

Competing financial interests

The authors declare no competing financial interests.